JOURNAL OF GEOPHYSICAL RESEARCH, VOL. 106, NO. C8, PAGES 16,929–16,946, AUGUST 15, 2001

Horizontal wave number spectra of temperature in the unstably stratified oceanic surface layer

H. W. Wijesekera, C. A. Paulson, and A. Huyer

College of Oceanic and Atmospheric Sciences, Oregon State University, Corvallis, Oregon, USA

Abstract. Horizontal wave number spectra of temperature in the unstably stratified oceanic surface layer were determined from measurements on a bow boom at a depth of 2 m. Spectra were estimated in the wavelength band from 2 m to 2 km, normalized in accordance with Monin-Obukhov similarity theory, and averaged in groups with similar stability parameter and fractional mixed layer depth. The shapes of the wave number-weighted oceanic spectra agree qualitatively with observed and modeled atmospheric spectra, including the wavelength of the peaks and the variation of peak wave number with stability. However, the peak spectral levels disagree by as much as a factor of two and the variation of spectral level with stability is in the opposite sense for the oceanic and atmospheric spectra. The wave number of the peak in the near neutral oceanic spectrum is similar to the wave number of the peak in the longitudinal velocity spectrum observed in the atmospheric surface layer, which is consistent with temperature acting as a passive tracer in near neutral conditions. The wave number of the peak in the free convection oceanic spectrum is similar to the wave number of the peak in the spectrum of vertical velocity observed in the atmospheric surface layer during free convection, which reflects the dynamical role played by temperature in a freely convecting boundary layer. The difference between oceanic and modeled near-neutral spectral levels at a wavelength of 2 m suggests that dissipation could be enhanced (up to a factor of three) by surface wave breaking.

1. Introduction

Investigations of turbulence in the oceanic surface layer are relatively rare in comparison to the numerous and extensive investigations of turbulence in the atmospheric surface layer over flat surfaces. The surface layer is defined here as the layer adjacent to the surface in which the vertical fluxes of momentum, heat, and mass are approximately independent of height. The thickness of the surface layer is about one tenth the thickness of the boundary layer or, typically, 1 to 10 m in the ocean and 10 to 100 m in the atmosphere.

A landmark investigation of turbulence in the atmospheric surface layer was carried out over flat, uniform terrain in Kansas during the summer of 1968. *Kaimal and Wyngaard* [1990] have summarized the Kansas experiment. When normalized in accordance with Monin-Obukhov (M-O) similarity theory, Kansas spectra of velocity and temperature reduce to a family of curves that depend on the M-O stability parameter ζ at low wave number and reduce to a single universal curve in the inertial subrange [*Kaimal et al.*, 1972; *Kaimal and Finnigan*, 1994].

Wave processes may affect the applicability of M-O similarity scaling in the oceanic surface layer. M-O scaling uses the dissipation rate ε of turbulent kinetic energy (TKE) to scale spectral levels in the surface layer and dissipation is usually estimated from TKE production. Breaking waves may increase ε in the oceanic surface layer above solid wall values, thereby calling into question the validity of M-O scaling. Several investigators [e.g., *Anis and Moum*, 1995; *Drennan et al.*, 1996; *Terray et al.*, 1996] find that ε may exceed the solid wall value by up to a factor of 10, but some observations agree with the solid wall value. To explain the observations of ε, *Terray et al.* [1996] have suggested a scaling for ε based on depth, significant wave height, and the rate of energy input from the wind to the waves. In this paper we will use M-O similarity theory and examine the scaled spectra for evidence of the effects of enhanced dissipation due to breaking waves.

The focus of this paper is on wave number spectra of turbulent temperature fluctuations measured in the unstably stratified oceanic surface layer. The underway

Paper number 2000JC000624.
0148-0227/01/2000JC000624$09.00

measurements were made from a bow boom in the western Pacific equatorial warm pool during November and December 1992 and January 1993 as part of the Coupled Ocean Atmospheric Response Experiment (COARE). A principal objective is to use the M-O framework to analyze the temperature spectra and to compare the results with spectra from the atmospheric surface layer. Platforms and instruments are described in section 2. The observations, including criteria for selection of 2-km segments for analysis, are discussed in section 3. M-O scaling for the surface layer is reviewed in section 4. The scaled temperature spectra, including a comparison with atmospheric temperature spectra, are presented in section 5, which also includes a discussion of the mechanisms that determine spectral shape. Conclusions are presented in section 6.

2. Platforms and Instruments

Measurements of surface layer temperature (T) and salinity (S) were made while the R/V *Wecoma* was steaming in a butterfly pattern (Figure 1) in the intensive flux array during the Intensive Observating Period (IOP) of COARE [*Huyer et al.*, 1997]. These measurements were made by Sea-Bird sensors mounted on an underwater boom which extended 2 m forward from the bow (Figure 2). Pressure was also measured on the bow boom, which was at a mean depth of 2 m. Data from the bow boom were recorded at a sampling rate of 8 Hz. At the mean ship speed of 4 m s^{-1} the spatial sampling rate was 2 cycles per meter (cpm). Because of the pitching motion of the ship, the bow sensors measured T and S at a variable depth centered at 2 m.

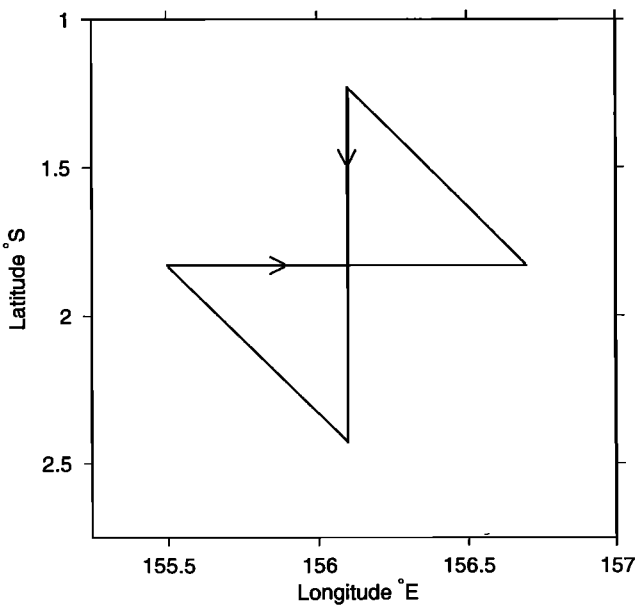

Figure 1. R/V *Wecoma*'s survey pattern. Arrows indicate the ship heading.

Measurements of T and S were also made by a SeaBird CTD in a Seasoar vehicle which undulated in the upper 300 m (Figure 2) with a cycling period of 8 to 12 min, corresponding to a horizontal distance between upcasts of 2 to 3 km. The sampling rate of the Seasoar CTD was 24 Hz [*Huyer et al.*, 1997]. We used spatially gridded Seasoar data (upcasts averaged vertically over 1 m and horizontally over 2 nautical miles (nm) along ship's track) to estimate mixed layer depths.

Meteorological measurements were made at several locations on *Wecoma* and averages were recorded at 1-min intervals. Two R. M. Young propeller anemometers mounted on each side of the ship's main mast measured wind speed and direction 21 m above the sea surface. For each 1-min interval the measurement by the best exposed anemometer was selected for analysis. Apart from the anemometers and a barometer, all other meteorological instruments were located at port, starboard and bow locations 8 m above the sea surface. Aspirated sensors manufactured by Vaisala and Rotronics measured air temperature and relative humidity. Pyranometers (Eppley PSP) and pyrgeometers (Eppley PIR) measured incoming shortwave and longwave radiation, respectively. Funnel gauges manufactured by R. M. Young measured rainfall accumulation by use of a capacitance technique. Rainfall rate was measured by an optical rain gauge (ORG) manufactured by Scientific Technology Inc. Ship heading and speed and GPS position were also recorded at 1-min intervals. Hourly meteorological observations were taken manually, which included sea temperature at a depth of 20 cm with a bucket thermometer.

3. Observations

The observations come from Cruise Legs 1 and 2 of the R/V *Wecoma* during the 4-month IOP of COARE. On average, winds were weak during the first leg (mid November to early December 1992) and there was net surface heating with little rain (Table A1). During the second leg (mid December 1992 to mid January 1993), there were westerly wind bursts, net surface cooling, and periods of heavy rainfall (Table A1). Average mixed layer depth determined from Seasoar upcasts was 16 m during Leg 1 and 29 m during Leg 2 [*Huyer et al.*, 1997]. Mixed layer depth is defined as the minimum depth at which the difference between density at that depth and the uppermost observation is equal to 0.01 kg m^{-3}. *Weller and Anderson* [1996] describe the surface meteorology and air-sea fluxes for the entire IOP.

3.1. Air-Sea Fluxes

The half-hour means of meteorological measurements from R/V *Wecoma* were used to estimate air-sea fluxes

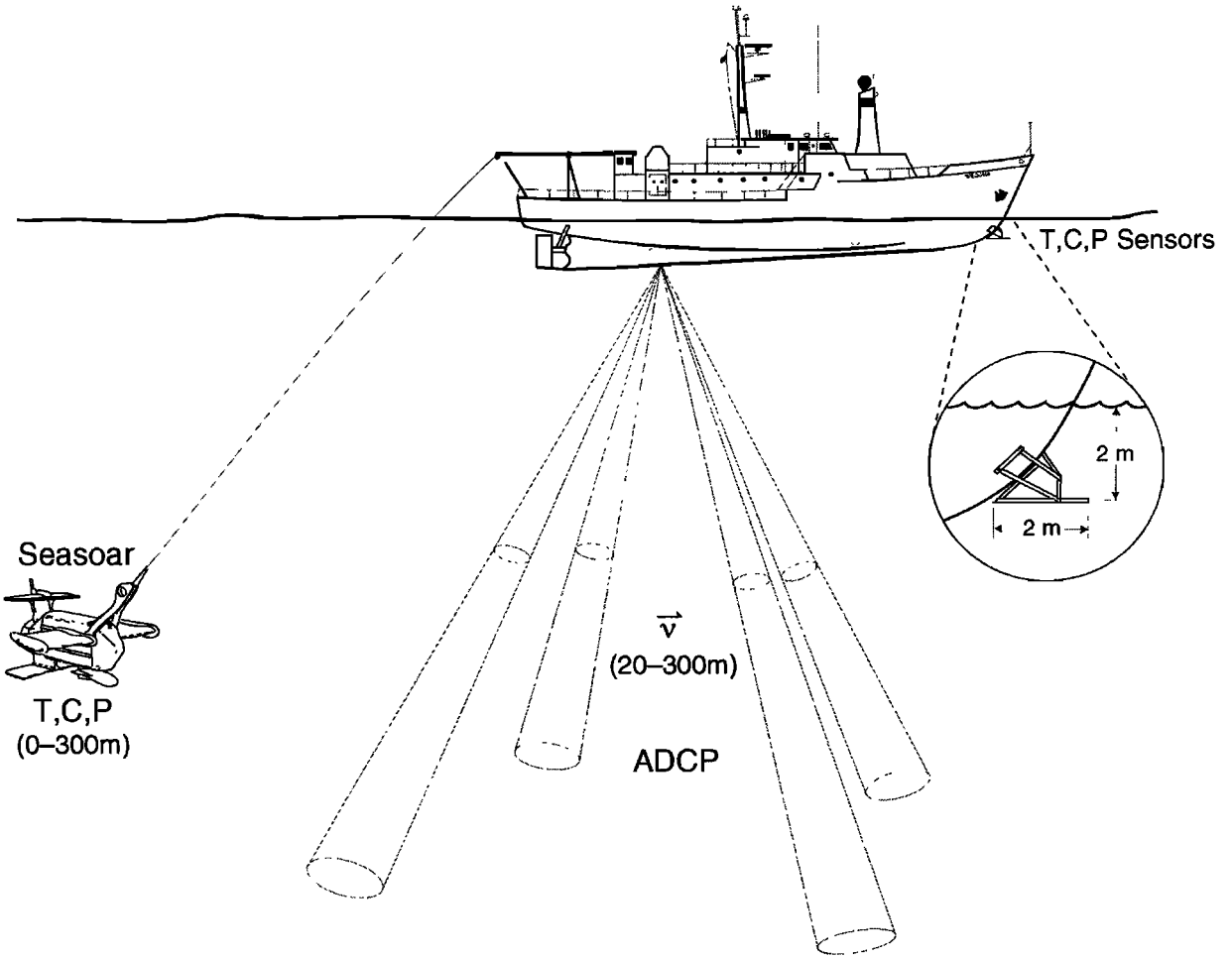

Figure 2. Schematic diagram of R/V *Wecoma* and measurements. Bow sensors (T, C, P) were attached to a bow boom at a depth 2 m below the water level. Wecoma was equipped with a shipboard acoustic Doppler current profiler (ADCP). Meteorological instruments, with the exception of anemometers, were located 8 m above the water line on a bow mast, atop the winch control station on the starboard side, and on a mast on the port side of the 01 deck. Propeller/vane anemometers were located 21 m above the waterline on both sides of the main mast. Seasoar was towed behind the ship.

of momentum, heat and water. The fluxes were estimated by use of Version 2.5 of the COARE bulk flux algorithm [*Fairall et al.*, 1996a,b; *Godfrey et al.*, 1998]. A surface albedo of 0.04 was used to compute net solar radiative flux. A surface emissivity of 0.97 was used to compute net longwave radiative flux. Fluxes, averaged over Legs 1 and 2, are given in Table A1 and are compared with averages over identical periods from the *MoanaWave* [*Fairall et al.*, 1996a]. The fluxes of momentum and sensible and latent heat from *MoanaWave* were primarily from eddy correlation measurements. Despite separations ranging up to 70 km the average fluxes from the two ships are in excellent agreement. Differences between total heat fluxes and their components do not exceed 6 W m^{-2} (see Appendix A for details).

3.2. Selection of Bow Data

Bow measurements of T and C at a mean depth of 2 m were analyzed to study the structure of the OBL during quasi-steady nighttime cooling. Segments of the measurement record were selected to minimize the effects of rainfall on density, to exclude periods when sensors were out of the water, to exclude contamination of conductivity measurements by air bubbles, and to exclude periods containing erroneous spikes in the temperature measurements. Observations from 11 nights (four from Leg 1 and seven from Leg 2) were chosen which contained a substantial amount of suitable data. This record was divided into segments of 512 s (2 km at 4 m s^{-1}). Individual segments were then accepted for analysis if they met the following criteria: (1) Downward short-wave radiation was less than

10 W m^{-2} (nighttime). (2) Net upward surface heat flux was greater than 100 W m^{-2} (surface cooling). (3) No rainfall was recorded during the hour containing the segment. (4) The ship was not making a turn during the segment. (5) The kurtosis of the conductivity derivative was less than 11. (6) The kurtosis of the temperature derivative was less than 11. (7) The turbulent density ratio (defined in Appendix B) was less than 0.64.

A discussion of the above criteria is given in Appendix B. A total of 306 2-km segments were accepted for analysis. Mixed layer depth (D) for each of the 306 segments was estimated from 1-dbar averaged Seasoar upcasts (see Appendix C for a description of the method).

3.3. Examples of Selected Bow Data

Time series plots of bow temperature, salinity and pressure from two of the total of 306 segments accepted for analysis are shown in Figures 3 and 4. Figure 3 shows a typical case of low wind forcing with a shallow mixed layer (15 m), and Figure 4 shows a typical case of moderately strong wind forcing with a deep mixed layer (65 m). Salinity fluctuations were weak and were contaminated due to salinity-spiking. Temperature fluctuations were as large as 0.02°C and exhibited small-scale frontal features, especially during high winds. Pressure fluctuations were less than 0.4 dbar when winds were weak (~2 m s^{-1}) and the ship was heading approximately perpendicular to the wind (Figure 3c). Pressure fluctuations exceeded 1.5 m when the ship was pitching during moderately strong winds (~10 m s^{-1}) (Figure 4c).

Band-averaged wave number spectra of the records shown in Figures 3 and 4 are plotted in Figure 5. Spectra were computed by use of a fast Fourier transform (FFT) algorithm with a boxcar window of 512 s. The Nyquist wavemumber was 1 cpm. The high wave number roll-off due to finite response time (0.07 s) [e.g., *Gregg et al.*, 1973] of the temperature sensor was corrected using a frequency domain response function (a double-pole filter); details of this correction are given by *Wijesekera et al.* [1999]. Each spectrum was smoothed by averaging over wave number bands spaced logarithmically (Figure 5).

Pressure spectra, $S_P(k)$ (Figure 5b) peaked at the pitching frequency (~0.1–0.2 Hz) of the ship, where k is horizontal wave number f/U_S, U_S is the average ship speed of 4 m s^{-1}, and f is the frequency in Hz. In most cases this spectral peak was well defined. However, the frequency and the magnitude of heaving depend on the

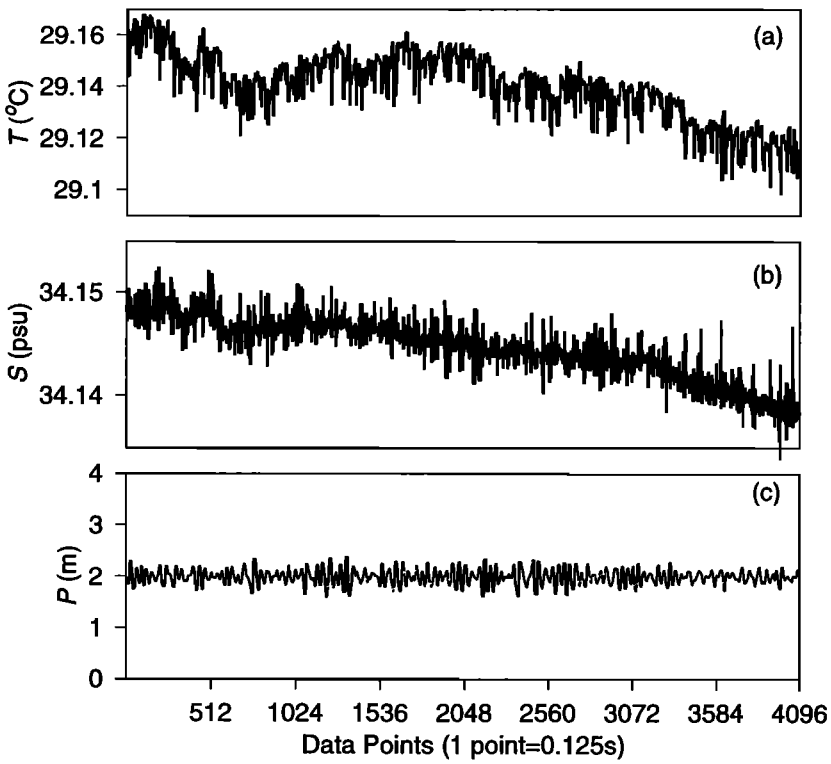

Figure 3. A typical bow segment during weak winds with a shallow mixed layer. The length of the record is 512 s (4096 data points) starting from 331.45297 UTC (January 1, 1992, 0000 GMT = 1 UTC). The 30-min averaged wind stress was $\tau = 0.014$ N m^{-2}, surface net heat flux $Q_s =$ 145 W m^{-2}, stability parameter $\zeta = -1.75$, and mixed layer depth $D = 15$ m.

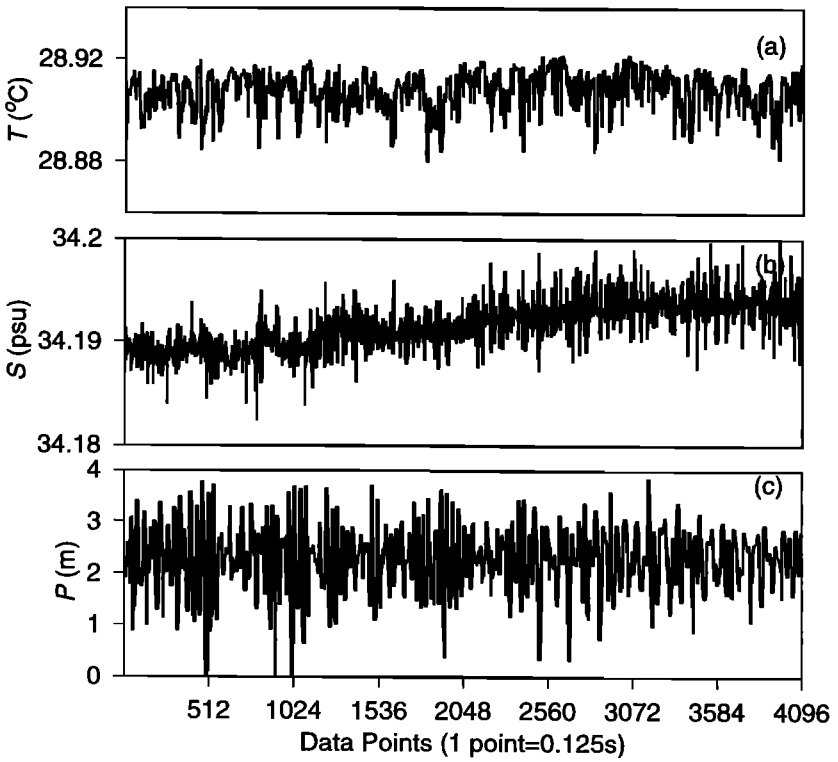

Figure 4. A typical bow segment during moderate winds with a deep mixed layer. The length of the record is 512 s (4096 data points) starting from 365.66722 UTC. The 30-min averaged wind stress was $\tau = 0.09$ N m^{-2}, surface net heat flux $Q_s = 265$ W m^{-2}, stability parameter $\zeta = -0.185$, and mixed layer depth $D = 65$ m.

relative angle between the ship and the waves, and the wave height and wave length (Figures 3c, 4c, and 5b).

Near-surface stratification can modify T or S spectra at pitching frequencies as a result of the ship motion, especially when near-surface vertical gradients of T and S are large. In such a case, T and S spectra will have a localized peak at the pitching frequency (or range of frequencies) along with high coherences between T and P, and S and P. As shown in Figure 5, the coherence between T and P was negligible, and there were no apparent peaks in the temperature spectrum ($S_T(k)$) at the pitching wave number ($\sim 5 \times 10^{-2}$ cpm) indicating that near-surface vertical gradients were weak and that their impact on the temperature spectra was insignificant.

Sample spectra of $T(S_T(k))$ indicate an approximate $-5/3$ spectral power law behavior for wave numbers greater than 0.07 cpm, and the spectral slope is less steep at lower wave numbers (Figure 5a). Although there is no clearly defined $-5/3$ range in the salinity spectrum ($S_S(k)$), it appears that $S_S(k)$ approaches the $-5/3$ range for k >0.5 cpm (Figure 5d), but the high wave number spectrum of S may be contaminated by noise.

4. Surface Layer Scaling

4.1. Monin-Obukhov Similarity

The spectra will be examined within the framework of the Monin-Obukhov (M-O) similarity hypothesis for the surface layer [*Monin and Obukhov,* 1954; see also *Wyngaard,* 1973]. This framework is often used to analyze spectra measured in the atmospheric surface layer [e.g., *Kaimal et al.,* 1972], and we will apply it to temperature spectra measured in the oceanic surface layer.

The surface layer is defined as the layer adjacent to the surface in which the vertical turbulent fluxes of momentum, heat and mass do not depart significantly (less than ~10%) from their surface values. The thickness of this layer is ~10% of the boundary layer thickness.

The requirement for constancy of the turbulent heat flux in the oceanic surface layer constrains the magnitude of solar irradiance at the surface to small values. The absorption of solar radiation is a strong function of depth in the upper ocean [e.g., *Paulson and Simpson,* 1977] which introduces vertical variations in the turbulent heat flux. All of the observations analyzed in this paper were taken at night; hence the requirement for small surface solar irradiance is easily fulfilled.

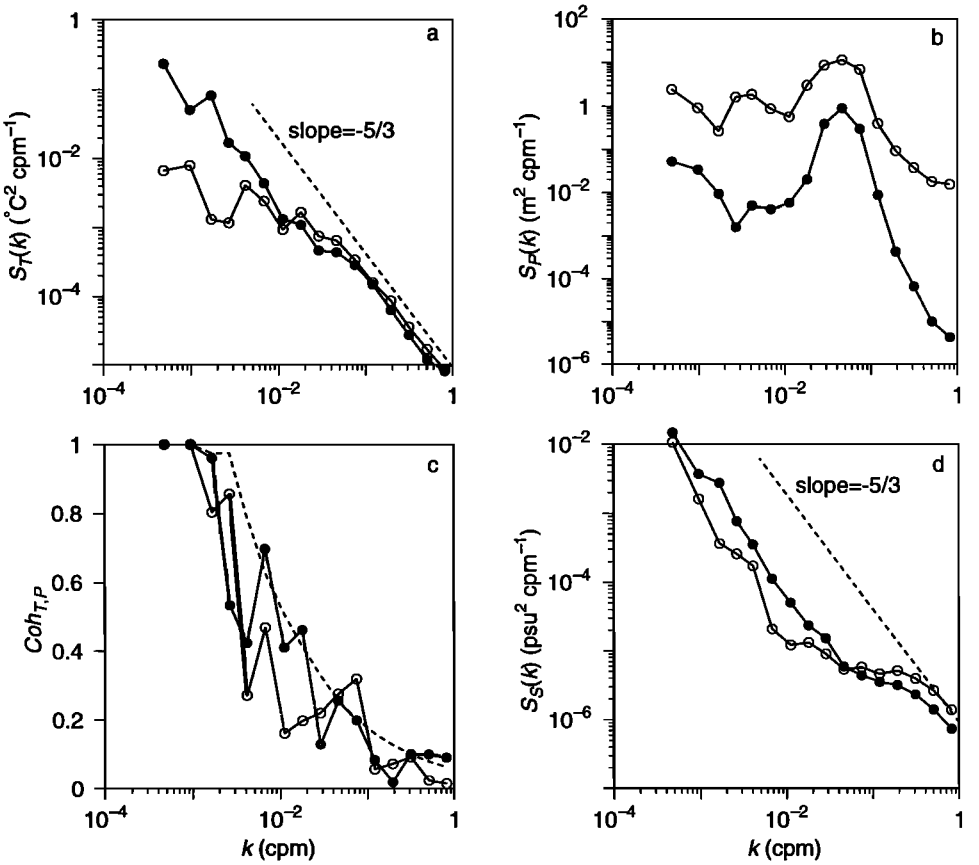

Figure 5. Spectra plotted versus wave number (cpm) for data shown in Figures 3 (solid circle), and 4 (open circle): (a) Temperature spectrum $S_T(k)$; the dashed line denotes the $-5/3$ spectral slope; (b) pressure spectra $S_P(k)$; (c) coherence spectrum between T and P, and (d) salinity spectrum $S_S(k)$ along with a dashed line denoting the $-5/3$ spectral slope.

A version of the M-O similarity hypothesis for the surface layer states that the turbulent structure of the energy-containing scales is determined by the group of variables $-\overline{uw}, \overline{w\rho}, g/\rho_0$, and z, where $-\overline{uw}$ is the covariance of the turbulent velocity components u and w, $\overline{w\rho}$ is the covariance of w and the turbulent density ρ, g is the acceleration due to gravity, and ρ_0 is a reference density. The overbars imply a time or space average. When dimensional analysis is applied to the above group of four variables (all constant in the surface layer except z), one independent non-dimensional parameter $\zeta = |z|/L$ is obtained, where

$$L = \frac{(-\overline{uw})^{3/2}}{\kappa \frac{g}{\rho_0} \overline{w\rho}} = -\frac{u_*^3}{\kappa J_b}, \tag{1}$$

where the von Karman constant κ (0.4) is traditionally included in the definition of L, J_b is the buoyancy flux, and u_* is the friction or scaling velocity ($u_* = (\tau/\rho_0)^{1/2}$ where τ is the wind stress). The parameter L is called the M-O length and $\zeta = |z|/L$ is the M-O stability parameter. We have chosen to use the absolute value of z in the numerator of ζ so that ζ is negative for unstable stratification and positive for stable stratification in both the atmospheric and oceanic surface layers (z positive or negative).

In the absence of precipitation, turbulent density fluctuations are determined primarily by turbulent temperature fluctuations θ, and density fluctuations can be approximated by $\rho = -\alpha\theta$ where α is the coefficient of thermal expansion. Contributions to the surface buoyancy flux due to brine rejection as the result of evaporation cannot be greater than 13% for the segments analyzed for this paper [see *Gill*, 1982, p. 37] and a typical value is 7%. In this paper we neglect the effect of brine rejection due to evaporation on the buoyancy flux and calculate J_b from the surface heat flux Q_s:

$$J_b = \frac{g\alpha Q_s}{\rho_0 C_p} = g\alpha\overline{w\theta}, \tag{2}$$

where C_p is the specific heat of seawater at constant pressure.

The M-O similarity hypothesis predicts that nondimensional characteristics of turbulent structure will be universal functions of ζ. As an example, consider the budget of turbulent kinetic energy (TKE) under sta-

tionary, horizontally homogeneous conditions with flux divergence terms neglected:

$$-\overline{uw}\frac{\partial U}{\partial z} - \frac{g}{\rho_0}\overline{w\rho} - \epsilon = 0, \tag{3}$$

where U is the mean velocity in the direction of the mean flow and ϵ is the dissipation rate of TKE. The first term in (3) represents the shear production of TKE, the second term represents buoyancy production, and the third term represents the dissipation of TKE into heat. The TKE equation (3) can be nondimensionalized through multiplication by $\kappa|z|/u_*^3$. The resulting nondimensional TKE equation is

$$\phi_m - \zeta - \phi_\epsilon = 0. \tag{4}$$

The first term of (4) is the nondimensional shear ϕ_m, and the third term is the nondimensional dissipation ϕ_ϵ. M-O predicts that both of these nondimensional variables are universal functions of ζ.

The budget of turbulent temperature variance (TTV, $\theta^2/2$) under stationary, horizontally homogeneous conditions and with neglect of a flux divergence term is [e.g., *Tennekes and Lumley,* 1983]:

$$-\overline{w\theta}\frac{\partial \Theta}{\partial z} - \chi_\theta = 0, \tag{5}$$

where χ_θ is the destruction rate of TTV due to molecular transport and Θ is the mean potential temperature. The first term in (5) is a production term, which is positive provided that the turbulent heat flux is downgradient. The TTV equation can be nondimensionalized through multiplication by $\kappa|z|/u_*\theta_*^2$ where the temperature scale θ_* is $\overline{w\theta}/u_*$. The resulting nondimensionalized TTV equation is

$$\phi_h - \phi_\chi = 0, \tag{6}$$

where ϕ_h is the nondimensional vertical temperature gradient and ϕ_χ is the nondimensional destruction rate of TTV.

The nondimensional groups introduced above are summarized below:

$$\phi_m = \frac{\kappa z}{u_*}\frac{\partial U}{\partial z}, \tag{7a}$$

$$\phi_h = \frac{\kappa z}{\theta_*}\frac{\partial \Theta}{\partial z}, \tag{7b}$$

$$\phi_\epsilon = \frac{\kappa z \epsilon}{u_*^3}, \tag{7c}$$

$$\phi_\chi = \frac{\kappa z \chi_\theta}{u_* \theta_*^2}. \tag{7d}$$

Observations in the atmospheric surface layer [e.g., *Businger et al.,* 1971; *Wyngaard and Cote,* 1971; *Dyer,* 1974] are in good agreement with the M-O prediction that the above nondimensional variables should be universal functions of ζ. We adopt the empirically determined functions which are in agreement with the results from several atmospheric surface layer field experiments [*Kaimal and Finnigan,* 1994]:

$$\phi_m = (1 - 16\zeta)^{-1/4} \qquad -2 \le \zeta \le 0, \tag{8a}$$

$$\phi_h = (1 - 16\zeta)^{-1/2} \qquad -2 \le \zeta \le 0, \tag{8b}$$

$$\phi_\epsilon = (1 + 0.5|\zeta|^{2/3})^{3/2} \qquad -2 \le \zeta \le 0. \tag{8c}$$

The functional form for ϕ_χ is taken to be identical to that for ϕ_h, which follows from the approximate TTV equation (5). *Kaimal and Finnigan* [1994] also give expressions for stable stratification.

4.2. Scaling Temperature Spectra

The temperature spectrum in the inertial subrange takes the form

$$S_T(k) = \beta_T \epsilon^{-1/3} \chi_\theta k^{-5/3}, \tag{9}$$

where $S_T(k)$ is the spectral level, k is wave number, and β_T is a universal dimensionless constant with a value of ~0.8 [*Kaimal et al.,* 1972]. The inertial subrange spectrum can be nondimensionalized by multiplication by k, division by θ_*^2, and use of the definitions of ϕ_ϵ and ϕ_χ to obtain

$$\frac{kS_T(k)}{\theta_*^2} = \frac{\beta_T}{(2\pi\kappa)^{2/3}} \phi_\epsilon^{-1/3} \phi_\chi n^{-2/3}, \tag{10}$$

where $n = k|z|$. The above may be written

$$\frac{kS_T(k)}{N_T} = \frac{\beta_T}{(2\pi\kappa)^{2/3}} n^{-2/3}, \tag{11}$$

where $N_T = \theta_*^2 \phi_\epsilon^{-1/3} \phi_\chi$. When observed spectra $kS_T(k)$ are normalized by N_T and plotted versus n in a log-log plot, they should collapse to a single line with slope $-2/3$ in the inertial subrange and departures from this line at lower wave numbers should be universal functions of ζ, as predicted by M-O similarity. This normalization will be used in the following section to analyze the oceanic spectra and to compare them with atmospheric surface layer spectra.

Peltier et al. [1996, hereinafter PWKB] have developed a model of spectra in the unstable atmospheric surface layer. The model has a single form for the two-dimensional spectrum of horizontal velocity, vertical velocity, and a scalar in the horizontal plane. Continuity is used to relate the vertical and horizontal velocity spectra. The spectra follow law of the wall and mixed layer scaling in the neutral and free convection limits, respectively. The normalized, one-dimensional PWKB temperature spectrum $S_T^P(n)$ can be summarized for the neutral and free convection limits as

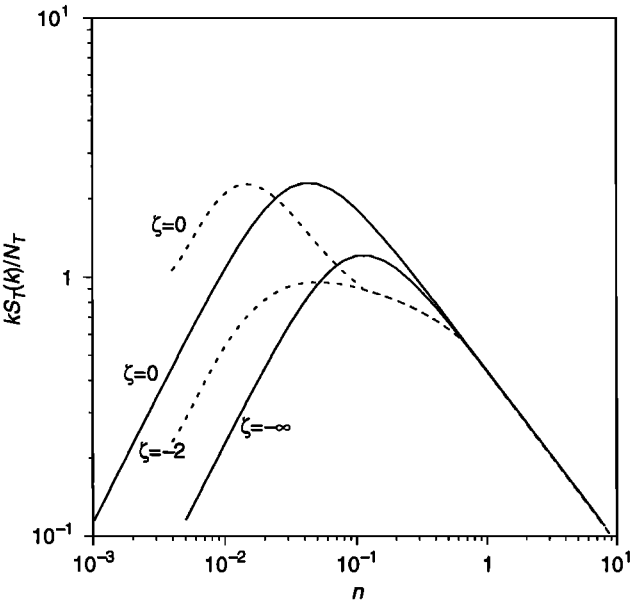

Figure 6. The PKWB normalized temperature spectra for free convection, $\zeta = -\infty$, and neutral stratification, $\zeta = 0$ (solid lines), along with temperature spectra observed during the Kansas experiment (dashed lines).

$$\frac{kS_T^P(k)}{N_T} = \frac{\beta_T}{(2\pi\kappa)^{2/3}} \frac{n}{(c_n + n^2)^{5/6}}, \qquad \zeta = 0 \quad (12a)$$

$$\frac{kS_T^P(k)}{N_T} = \frac{\beta_T}{(2\pi\kappa)^{2/3}} \frac{n}{(c_f + n^2)^{5/6}}, \qquad \zeta = -\infty \quad (12b)$$

where $\beta_T = 0.8$, $\kappa = 0.4$, $c_n = 0.05$, and $c_f = 0.34$. Note that for $n >> 1$,

$$\frac{kS_T^P(k)}{N_T} = \frac{\beta_T}{(2\pi\kappa)^{2/3}} n^{-2/3}. \qquad (13)$$

The PKWB normalized temperature spectra are shown in Figure 6 together with temperature spectra observed during the Kansas experiment [*Kaimal et al.*, 1972]. The observed and modeled spectra agree in the -2/3 range as required by the normalization. For neutral stratification the magnitude of the peaks of the Kansas and PKWB spectra are similar, but the wave number of the neutral PKWB spectrum is a factor of 3 larger than the corresponding wave number of the Kansas spectrum. The low wave number slopes of the two spectra are very similar. It is important to note that the neutral Kansas spectrum shown is for slightly unstable conditions ($\zeta = -0$) and that there was considerable scatter of the spectral estimates within the range of stability shown. Nevertheless, *Kaimal et al.* [1972, p.572] note that "the tendency of the logarithmic spectral peak to shift towards increasingly larger n with increasing instability is real." The difference in behavior of the Kansas and PKWB spectra may be partially due to the Kansas spectrum being affected by processes unrelated to horizontally uniform boundary layer turbulence. One possibility is the entrainment of low wave number temperature fluctuations into the boundary layer from the overlying atmosphere. The idealized nature of the model spectrum may also contribute to differences with observations. In the next section we compare the one-dimensional form of PWKBs scalar spectrum with the oceanic temperature spectra.

5. Spectra

5.1. Averaged Spectra

The temperature spectrum for each of the 306 segments was computed and nondimensionalized by multplying the spectral level by the ratio of wave number k to the normalization factor N_T (see previous section) and by multiplying wave number by the depth of the measurement (2 m). These normalized spectra are hereafter referred to as "n spectra." The values of N_T were determined from estimates of air-sea fluxes (see above).

Fractional mixed layer depth $|z|/D$ and stability ζ for the spectrum from each of the segments cover a broad range of values with $|z|/D$ ranging from 0.03 to 0.2 and ζ from -0.04 to -4 (Figure 7). The n spectra were grouped by $|z|/D$, ζ, and qualitative similarity in spectral shape into six main groups denoted by A through F as shown in Figure 7. The main groups were further divided into two or three subgroups with smaller intervals of stability and fractional mixed layer depth (Figure 7).

Averaged n spectra for each of the subgroups are plotted in Figure 8 together with PWKB model spectra for $\zeta = 0$ (neutral stratification) and $\zeta = -\infty$ (free convection). There is fair qualitative agreement between the PWKB model and the observed spectra for nondimensional wave numbers in the band from 0.03 to 1, essentially the turbulent energy containing range of the spectra characterized by a peak centered at wave numbers varying from 0.03 to 0.1. The observed spectral level at $n = 0.03$ of every subgroup falls between the levels of the modeled neutral and free convection spectra. For the groups closest to neutral (Figure 8f) the wave number of the peak is close to that of the modeled neutral spectrum, but the maximum spectral level is very close to the peak of the modeled free convection spectrum. The observed peak in the near-neutral spectrum also appears to be broader than the model. For the most unstable group (Figure 8a) the spectral levels lie above the modeled free convection spectrum but there is good agreement in the location and width of the peak. In the wave number band below 0.03, there is large variation in spectral level, which is unrelated to local production of turbulent temperature fluctuations (term 1 in (5)).

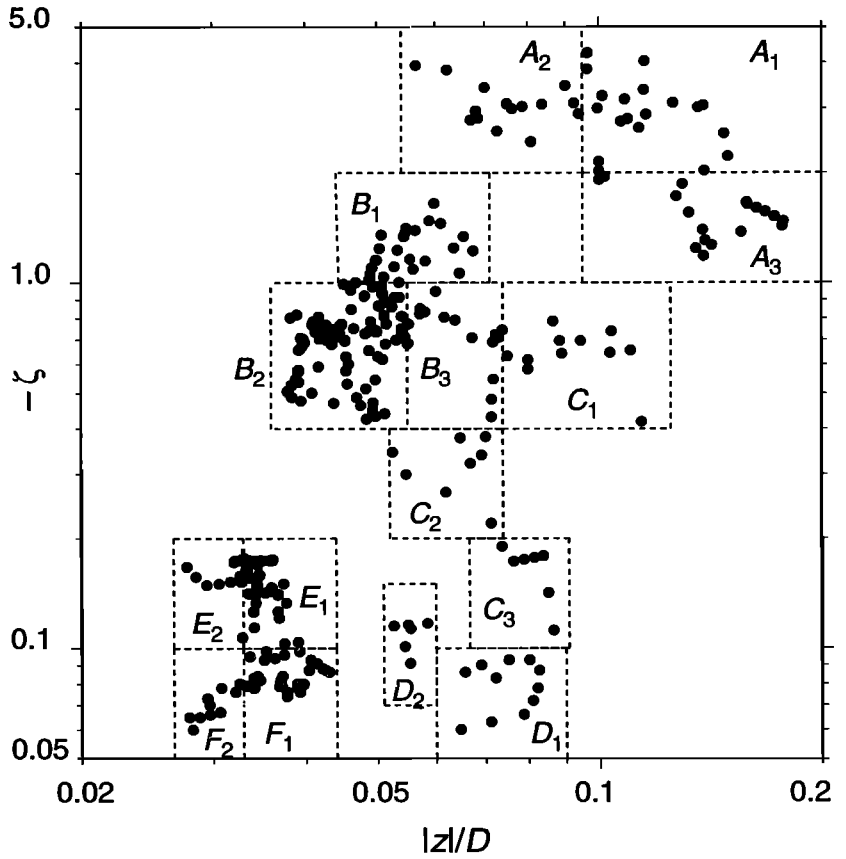

Figure 7. Stability parameter (ζ) versus fractional mixed layer depth ($|z|/D$) for each of the 306 spectra. The spectra are grouped, as shown by the dashed lines and labels, to obtain average spectra for restricted ranges of ζ and $|z|/D$.

To summarize the observed spectral shapes at near neutral and highly unstable conditions, curves have been fitted to spectra from the nearest neutral and most highly unstable subgroups (F_2 and A_2 in Figures 7 and 8). These curves are plotted in Figure 9 together with the PWKB model in both log-log and log-linear form. The log-linear plot (Figure 9b) is variance-preserving, i.e., equal areas under the curve contribute equally to the total variance. In determining the fits, spectral estimates at the lowest wave numbers were ignored and the spectral shape at low wave number was assumed to be the same as the PWKB model (slope = + 1 in a log-log plot). The spectral estimates used to determine the fits are plotted in Figure 9. The wave number of the peak of the highly unstable oceanic spectrum agrees with the PWKB model, but the observed spectral level is 40% higher. The oceanic near-neutral spectrum has a broader peak than the model and the observed peak is at slightly lower wave number than the model. The modeled neutral spectral level exceeds the observed near-neutral spectral level by a factor of 2. For the observations the normalized TTV for the most unstable case is 17% larger than the TTV for the near-neutral case.

The near neutral and highly unstable spectra are compared in Figure 10 with temperature spectra measured in the atmospheric boundary layer over uniform terrain in Kansas [*Kaimal et al.*, 1972]. The wave numbers of the peaks of the oceanic and atmospheric near-neutral spectra are similar, but the spectral shapes differ and the atmospheric peak spectral level exceeds the peak oceanic spectral level by more than a factor of 2. The wave numbers of the peaks of the highly unstable oceanic and atmospheric spectra are similar but the oceanic spectrum is narrower and the oceanic peak spectral level is 75% larger than the Kansas spectrum. One possible reason for differences between the oceanic and atmospheric spectra is that the fractional boundary layer height $|z|/D$ at which the Kansas measurements were made was smaller than 0.03 for the oceanic near neutral case and 0.08 for the oceanic highly unstable case. If one assumes a typical daytime boundary thickness of 1000 m, the range of $|z|/D$ for the Kansas spectra was 0.006 to 0.02.

5.2. Turbulence Mechanisms

Variation in spectral shape as a function of stability may give insight into underlying turbulence mecha-

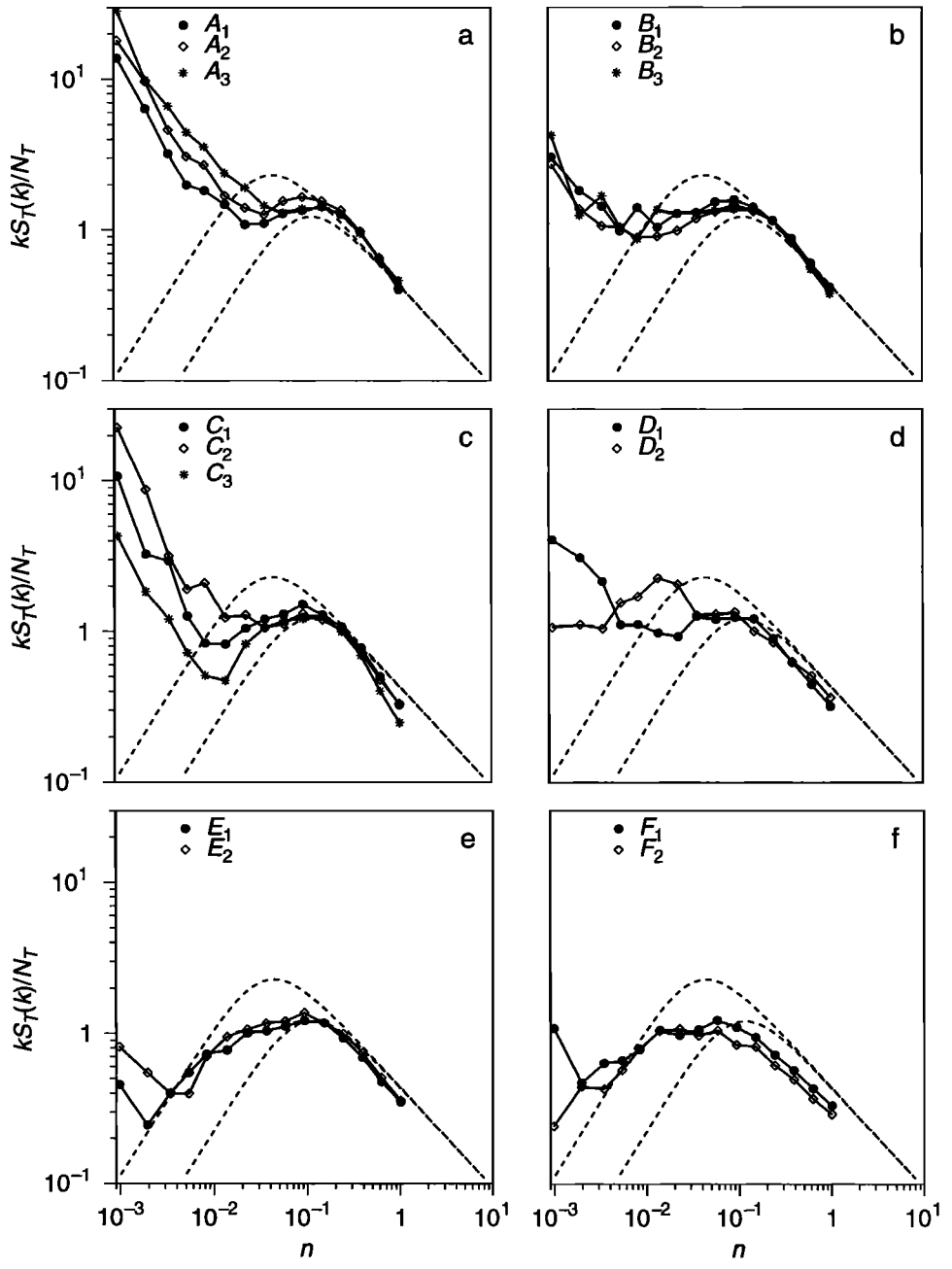

Figure 8. Average normalized spectra, $kS_T(k)/N_T$ plotted versus nondimensional wave number, $n = k|z|$, for different $|z|/D$ and ζ groups (see Figure 7), where N_T is the normalization factor defined following (11). The neutral and free convective limits of PWKB spectra are plotted in dashed lines.

nisms. In this section we focus on differences between spectra from the most unstable and the most nearly neutral stability ranges (Figure 9). Variations in spectral shape will be ascribed to differences in the production of TKE and TTV for near neutral and free convection conditions.

At wave numbers in excess of n=0.2, where the PWKB modeled spectral slope is close to -2/3, the near neutral and most unstable spectra depart from the model in opposite ways (Figure 9). Spectral levels from the group with most nearly neutral stratification fall below the model with slopes less steep than -2/3 (Figure 9a). In contrast, spectral levels from the most unstable group are above the model at n=0.3 and the slopes at the highest wave numbers are steeper than -2/3 (Figure 9a). To further illustrate this behavior, the ratio of observed to modeled spectral level is plotted as a function of ζ in Figure 11. The results show an increase of the ratio

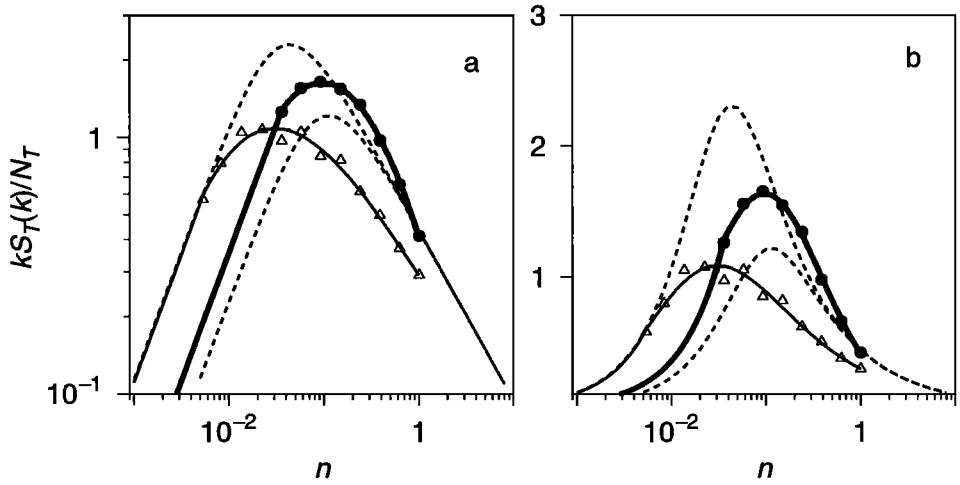

Figure 9. Near-neutral (F2 in Figure 8, open triangles) and most unstabl (A2 in Figure 8, closed circles) spectra plotted together with the PWKB spectra; (a) in log-log form and (b) in log-linear variance preserving form. The light and heavy solid lines are fits to the observations assuming a +1 slope at low wave numbers. The PWKB spectrum with the highest peak is the neutral spectrum.

with increasing instability both at n equal 1 and 0.39. At n=0.39 the ratio ranges from 0.6 at ζ=-0.07 to 1.1 at ζ=-2. The variation of mean $|z|/D$ as a function of ζ is small except for the three points with ζ in excess of 1.1, which shows that the fractional depth of the mixed layer does not strongly influence the results (Figure 11). The variation of normalized spectral level as a function of stability at $n = 1$ (wavelength = 2 m) indicates that conditions are not locally isotropic at that wave number. If one were to extrapolate the near neutral spectra in Figure 9a to higher wave numbers, the extrapolated spectrum would intersect the model spectrum at approximately $n = 10$ (a wavelength of 0.2 m). Hence necessary conditions for local isotropy require n to be 10 or greater.

When stratification is near neutral, the heat flux is small and the production of TKE is dominated by shear production (term 1 in (4)). Temperature does not play a significant dynamical role in near-neutral conditions but simply acts as a tracer. The production of TKE goes initially into the downstream component and part of this energy is then transferred to the vertical and lateral components by the action of pressure forces [e.g., *Lumley and Panofsky,* 1964]. TKE is also transferred from large to small scales which tend to become isotropic as scale size decreases. Because temperature acts as a tracer in near neutral conditions, we expect that the correlation between temperature and downstream velocity fluctuations would be high; *Kaimal et al.* [1972] reported a correlation coefficient of -0.56 for ζ ranging from 0 to -0.1. This can be compared with the correlation coefficient for temperature and vertical velocity, which was 0.37 for the same stability range.

Because temperature and downstream velocity are highly correlated in near neutral conditions, we might expect that the spectrum of temperature and longitudinal velocity would be similar in shape for these conditions. *Kaimal et al.* [1976] found that the wavelength corresponding to the maximum in the spectral level of longitudinal velocity is ~1.5 D. The mean D for our most nearly neutral spectrum is 67 m, which yields a prediction of 100 m for the wavelength of the maximum or $n = 0.02$ after scaling. The maximum in the fitted temperature spectrum for near-neutral conditions is at $n = 0.03$ (Figure 9), very close to the prediction for the longitudinal velocity spectrum. The two numbers agree within the range of their respective uncertainties.

When conditions are highly unstable, ($\zeta < -1$) buoyancy production dominates in the production of TKE (term 2 in (4)). For these conditions, temperature plays a dynamical role through the action of gravity on density fluctuations. When turbulence is driven primarily by surface cooling, the energy containing range of the turbulent velocity spectrum is anisotropic with enhanced vertical velocity compared to the same magnitude of neutrally stratified shear production [e.g., *Peltier et al.,* 1996]. This occurs because the production of TKE driven by surface cooling goes initially into the vertical velocity component from where it is transferred by turbulent pressure forces into the horizontal components [see, e.g., *Lumley and Panofsky,* 1964]. Given the dynamical link and the observed correlation between temperature and vertical velocity fluctuations in an unstably stratified boundary layer, one might expect an increase in the normalized horizontal wave number spectrum of temperature when stability changes from

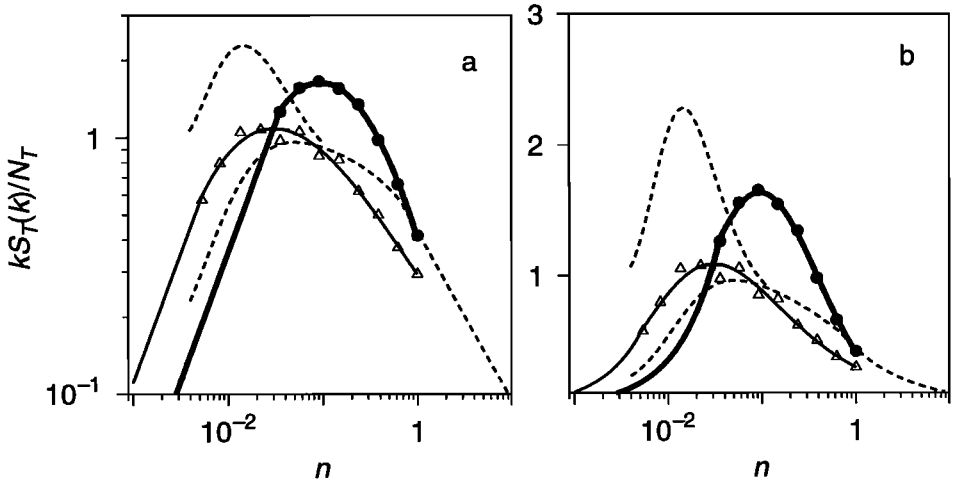

Figure 10. Same as Figure 9 except that the dashed lines are the near-neutra (highest peak) and most unstable Kansas temperature spectra.

near neutral to highly unstable. *Kaimal et al.* [1972] report a correlation coefficient of 0.59 for temperature and vertical velocity for ζ in the range -1.0 to -2.0. The correlation coefficient for temperature and downstream velocity in the same stability range was -0.18. Given the high correlation between temperature and vertical velocity for highly unstable conditions, one would expect the shape of the temperature and vertical velocity spectra to be similar. *Kaimal et al.* [1972] report that the wave number of the maximum in the vertical velocity spectrum approaches a constant 0.15 when ζ approaches -2 and this compares favorably with the wave number of the peak in the most unstable oceanic temperature spectrum, which is $n = 0.1$.

5.3. Effect of Surface Gravity Waves

Several researchers [e.g., *Agrawal et al.*, 1992; *Anis and Moum*, 1995; *Drennan et al.*, 1996; *Terray et al.*, 1996; *Soloviev et al.*, 1999] report that the dissipation rate ϵ in the wave boundary layer is up to an order of magnitude larger than predictions from similarity

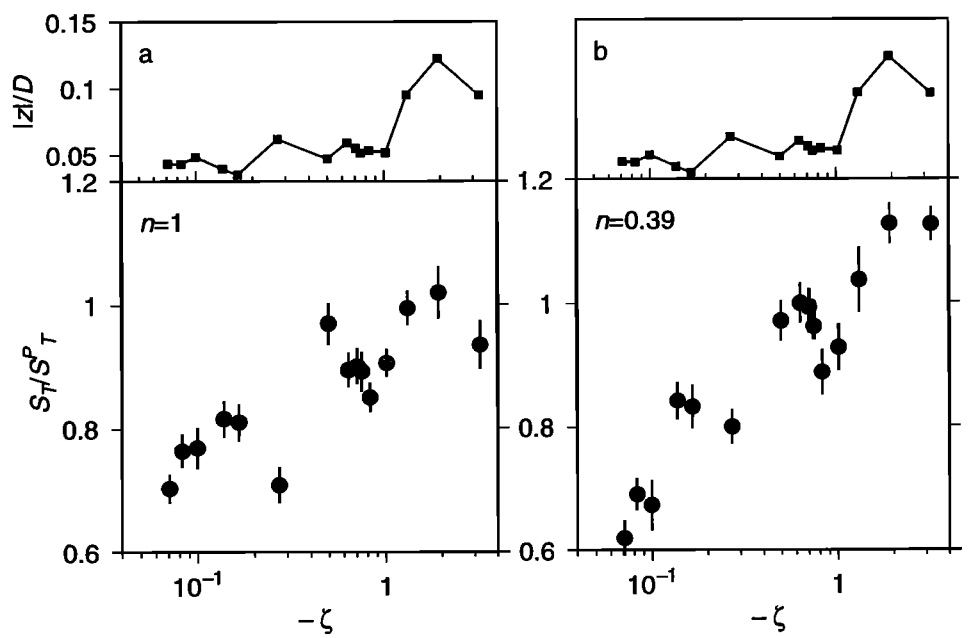

Figure 11. Ratio of spectral level S_T/S_T^P averaged within intervals of ζ and plotted versus ζ, where S_T^P is the PWKB temperature spectrum: (a) at $n = 1$ and (b) at $n = 0.39$. Thin vertical lines associated with each solid circle denote standard errors. The top panels show the average $|z|/D$ versus ζ.

scaling for the surface layer adjacent to a solid surface (equations (7c) and (8c)). The enhanced dissipation is ascribed to the wave generation/dissipation process. The waves extract energy from the wind, thereby reducing dissipation in the atmospheric boundary layer below the extraction level compared to that over a solid surface. When the waves break (or dissipate), they enhance dissipation in the oceanic boundary layer. One would expect that the effects of wave generation/dissipation would be largest for high winds.

Enhancement of dissipation due to waves was neglected in the estimates of ϵ used to scale the temperature spectra (equations (8c) and (11)). The spectral level of the PWKB model lies ~50% above the spectral estimate at $n = 1$ for the most nearly neutral case (Figure 9a). If the difference is due entirely to the neglect of wave enhanced dissipation, ϵ would have to be increased by a factor of 3 to force agreement between the observations and the model spectrum. An enhancement factor of 3 agrees with the average reported by *Soloviev et al.* [1999] for observations at a depth of 1.7 m with wind speed ranging from 6 to 16 m s^{-1}. High winds would accentuate wave generation/dissipation processes and our most nearly neutral case is associated with the highest observed wind, which averaged 10 m s^{-1}. Nevertheless, the factor of three should be regarded as an upper bound on the wave enhancement factor for dissipation because the observed spectral slope at $n = 1$ is less steep than -2/3 and the difference could therefore alternatively be attributed to lack of isotropy.

6. Conclusions

Underway measurements of temperature from a bow boom at a depth of 2 m have been analyzed to determine spectral characteristics in the wavelength band from 2 m to 2 km. A total of 306 2-km segments were selected for analysis. The criteria for selection included negligible solar insolation (nighttime), surface cooling greater than 100 W m^{-2}, and negligible effect of salinity on density fluctuations. The spectra were averaged in groups having similar Monin-Obukhov stability parameter ζ and similar fractional boundary layer depth $|z|/D$; mean group values of ζ ranged from -0.07 to -3 and mean group $|z|/D$ ranged from 0.03 to 0.14. The spectral levels were multiplied by wave number k and scaled following M-O similarity; wave number was normalized through multiplication by the depth of the measurement.

To first order, a log-log plot of the wave number weighted turbulent temperature spectrum in the oceanic surface layer has a +1 slope at low wave numbers, a -2/3 slope at high wave numbers (characteristic of an intertial subrange) and a peak in between (Figures 8 and 9). This schematic spectrum ignores high spectral levels at low wave numbers that are not due to local turbulent production but are thought to be associated with the mesoscale eddy field.

The normalized turbulent temperature spectrum varies as a function of stability ζ. The average spectrum from the near-neutral group ($\zeta = -0.07$) has a peak at $n = 0.03$ (Figure 9) which corresponds to a wavelength of 30 times the depth of the measurement. The spectral slope of the near neutral spectrum is less steep than -2/3 at $n = 1$, indicating that conditions are not locally isotropic at that wave number. The average spectrum from the most unstable group ($\zeta = -3$, which approximates free convection) has a peak at $n = 0.1$ (wavelength 10 times the depth of the measurement). The spectral slope of the free convection spectrum is steeper than -2/3 at $n = 1$. In free convection (surface cooling with negligible wind stress), the horizontal wave number spectrum of temperature is determined by the structure of descending plumes of cool water and ascending plumes of warm water. The characteristic separation of these plumes is 10 m at a depth of 2 m based on the wave number of the peak in the free convection spectrum.

The oceanic near-neutral and free convection spectra were compared with the PWKB model spectrum [*Peltier et al.*, 1996]. The wave numbers of the peaks of the oceanic near neutral and free convection spectra agree with the model but the spectral levels of the peaks disagree by as much as a factor of 2 (Figure 9). Moreover, the oceanic peak spectral levels increase with increasing instability while the reverse is true for the model. The normalized oceanic free convection TTV exceeds the near neutral oceanic TTV by 17% while the model free convection TTV is 52% less than the model near neutral TTV (Figure 9b).

The oceanic spectra were also compared with atmospheric temperature spectra observed over flat terrain in Kansas [*Kaimal et. al.*, 1972]. The wave number of the peaks of the oceanic near neutral and free convection spectra are in fair agreement with the Kansas spectra but the spectral levels of the peaks differ by up to a factor of 2 (Figure 10). The spectral level of the peak in the oceanic free convection spectrum exceeds the spectral level of the Kansas spectrum by 70%. In contrast, the spectral level of the peak in the oceanic near neutral spectrum is one-half the magnitude of the peak in the Kansas near neutral spectrum. A possible reason for the difference is that the fractional boundary layer heights at which the Kansas measurements were made may have been as much as an order of magnitude smaller than the corresponding oceanic fractional depths. It is also possible that near-neutral Kansas spectral levels in the low wave number range may have been overestimated because of entrainment of temperature fluctuations into the boundary layer.

Mechanisms for the production of TKE and TTV yield insight into the shape of turbulent temperature spectra. For near neutral stratification, temperature acts as a passive tracer of fluid motion with the prediction that the shape of the temperature spectrum will be similar to the longitudinal velocity spectrum. The *Kaimal et al.* [1972] expression for the wave number of the peak in the longitudinal velocity spectrum agrees with the wave number of the peak in the near-neutral oceanic temperature spectrum. For free convection conditions, TKE is produced by the action of gravity on density fluctuations and one expects a high correlation between vertical velocity and temperature. Hence one might also expect similarity between the shape of the vertical velocity and temperature spectra. *Kaimal et al.* [1972] report than the wave number n of the peak in the vertical velocity spectrum approaches a constant 0.2 for large values of $-\zeta$ and this compares favorably with $n = 0.1$ for the peak in the oceanic free convection spectrum.

The spectral level of the PKWB model lies about 50% above the oceanic spectral estimate for the most nearly neutral case at $n = 1$ (Figure 9a). If the difference were due entirely to neglect of enhanced dissipation due to wave breaking, ϵ would have to be increased by a factor of 3 to force agreement. An enhancement factor of 3 agrees with the average reported by *Soloviev et al.* [1999] for observations at a depth of 1.7 m with wind speed ranging from 6 to 16 m s^{-1}. An enhancement factor of 3 for the observations reported here should be regarded as an upper bound because the spectral slope at $n = 1$ is less steep than -2/3 and the difference may at least partially be attributed to a lack of isotropy.

Appendix A: Air-Sea Flux Comparison

The accuracy of the meteorological measurements is illustrated by a comparison of averages over Legs 1 and 2 from R/V *Wecoma* and R/V *Moana Wave* (Table A1). The *Moana Wave* was located near the center of the Wecomas 130-km butterfly pattern. Despite spatial separation of up to 70 km, the differences between averaged measurements from the two ships are small. The leg averages for *Wecoma* were constructed by first computing half-hour means from the 1-min averages and then computing an average for each leg. Leg averages for *Moana Wave* were computed from hourly means. Individual variables were usually measured by more than one instrument on *Wecoma*. Measurements from the best performing and best exposed instruments were selected for the half-hour averages. Calibrations were from the manufacturers of the instruments or based on lab calibrations. For some instruments, calibrations were corrected to force agreement between measurements of the same variable by different instruments on *Wecoma*. Calibrations were not modified to force agreement between the measurements from the two ships. However, insight into the performance of the instruments on *Wecoma* resulted from side-by-side comparison with other ships, including *Moana Wave* [*Godfrey et al.*, 1998]. The ef-

Table 1. Average near-surface variables and air-sea fluxes measured from R/V *MoanaWave* [*Fairall et al.*, 1996a,b] and R/V *Wecoma* during Legs 1 and 2 of COARE.[a]

	Leg 1			Leg 2		
	MW	Wec	MW-Wec	MW	Wec	MW-Wec
Wind speed, m s^{-1}	3.4	3.2	0.2	5.7	5.9	-0.2
Wind direction, deg	88.7	87.4	1.3	127.2	129.8	-2.6
Specific humidity, g kg^{-1}	19.0	18.3	0.7	18.3	18.4	-0.1
Air temperature, °C	28.0	28.4	-0.4	27.4	27.5	-0.1
Near-surface temperature, °C	29.5	29.6	-0.1	28.9	29.0	-0.1
Wind stress, N m^{-2}	.021	.017	-.004	.064	.064	.000
Net solar radiation, W m^{-2}	-225	-223	-2	-162	-168	6
Net longwave radition, W m^{-2}	63	62	1	52	56	-4
Latent heat flux, W m^{-2}	90	86	4	119	120	-1
Sensible heat flux, W m^{-2}	6.0	4.6	1.4	8.4	9.1	-0.7
Total heat flux, W m^{-2}	-66	-70	4	17	17	0
Rain rate, ORG, mm da^{-1}	3.3	3.6	-0.3	16.4	17.8	-1.4
Rain rate, funnel, mm da^{-1}		2.3			11.6	

[a]The *Wecoma* steamed around a 130-km butterfly pattern and the *MoanaWave* was located near the center of this pattern [*Huyer et al.*, 1997]. Leg 1 includes the period from November 14 to December 2, 1993, and Leg 2 is from December 20, 1992 to January 11, 1993. *MoanaWave* fluxes of momentum and sensible and latent heat were a combination of eddy correlation and version 2.5 of the COARE bulk flux algorithm, while corresponding fluxes from *Wecoma* were solely from the bulk flux algorithm.

fects of solar heating of the pyrgeometer on the measurement of incoming longwave radiation were removed by using an algorithm proposed by *Alados-Arboledas et al.* [1988]. Optical rain gauge measurements were corrected for a lack of cosine response. The difference in rain rate estimated from the optical and funnel gauges is due to under measurement by the funnel gauges due to their interference with the air flow around the gauge [*Koshmieder,* 1934].

Appendix B: Selection Criteria

The first four criteria listed in section 3.2 make use of the air-sea fluxes and navigation measured on the *Wecoma.* The first criterion ensures that the upper ocean was not affected by subsurface absorption of solar radiation. The second criterion requires that surface cooling was significant. The third criterion ensures that rainfall did not contribute to the surface buoyancy flux while the segment was measured. The fourth criterion guarantees that wave number spectra and other statistics are from measurements in a single direction.

The fifth criterion is used to exclude segments during which the bow sensors were out of the water or air bubbles were present at the sensors. Because of the pitching motion of the ship, the bow sensors measured T and C at variable depths centered at a mean depth of 2 m. When surface waves were sufficiently large, the sensors came out of the water, especially when the ship was headed into the wind. Even if the sensors did not break the surface, the measurements could have been affected by the presence of air bubbles associated with breaking waves. The momentary introduction of air into the conductivity cell, either due to bubbles or breaking the surface, caused a large negative spike in the conductivity record. The presence of such spikes results in an abnormally high value of the kurtosis, $K_{C'}$, of $\Delta C/\Delta x$ defined by

$$K_{C'} = \frac{1}{M}\sum_{j=1}^{M}\left[\frac{C'_j - \overline{C'}}{\sigma_{C'}}\right]^4, \qquad \text{(B1)}$$

where $M(= 4096)$ is the number of samples in a given segment. C' denotes the small scale gradient $\Delta C/\Delta x$ (Δx=0.5 m), the overbar denotes the average of C' over the segment, and $\sigma_{C'}$ denotes the standard deviation of C'. The kurtosis of the conductivity gradient varied between 5 and 935 with a mode of 7. The histogram of $K_{C'}$ (Figure B1) shows an increase in the number of segments with values larger than 11 (Figure B1) which we ascribe to air in the conductivity cell. Segments for which $K_{C'}$ is greater than 11 were therefore rejected. Examination of the histogram of $K_{T'}$ (defined as in (B1), Figure B1) lends further support to this criterion. The histogram shows no segments with $K_{T'}$ in the range

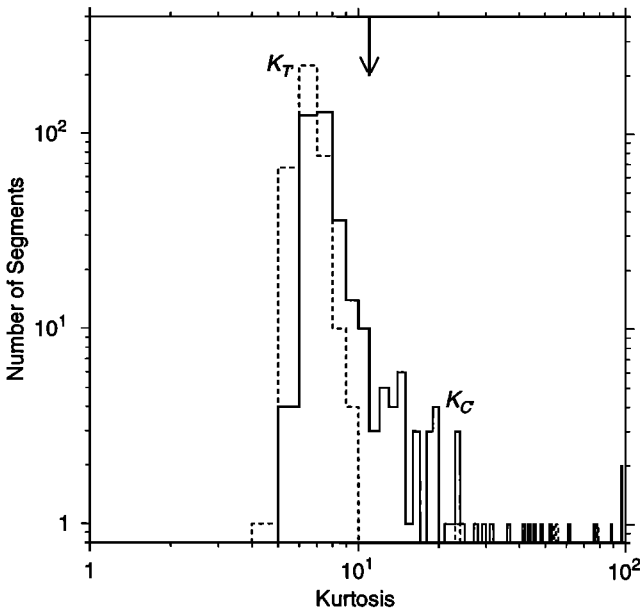

Figure B1. Histograms of Kurtosis estimated from (B1). The dashed line denotes the kurtosis of $\Delta T'/\Delta x(K_{T'})$ and the solid line denotes the kurtosis of $\Delta C'/\Delta x(K_{C'})$. Kurtosis values vary from 4 to 935; 2-km segments with Kurtosis less than 100 are plotted here. The value $K_{C'} = 11$ is marked by a downward arrow to indicate the criterion for acceptance of segments based on $K_{C'}$.

from 12 to 20, which can be interpreted as the negligible effect of bubbles on the measurement of T. However there are segments with values of $K_{T'}$ greater than 20 which is caused by sudden changes in temperature when the sensor breaks the surface and by erroneous spikes in the temperature record. The mode of the histogram of $K_{T'}$ has a slightly lower value than the mode of the histogram of $K_{C'}$. The difference is consistent with the conductivity cell having a faster response time than the temperature sensor [*Gregg et al.,* 1973; *Gregg and Hess,* 1985; *Lueck at al.,* 1977; *Morison et al.,* 1994].

The sixth criterion is used to exclude segments that contain erroneous spikes in temperature. Application of this criterion (after applying the previous five criteria) excluded three segments. The kurtosis of the temperature derivative was greater than 50 for all of these segments, a clear indication of erroneous data (see Figure B1).

The seventh criterion minimizes the effect of salinity variations, due primarily to rainfall, on density. Criterion 4 rejects segments during which rain may have fallen, but near-surface salinity anomalies caused by rainfall may persist [e.g., *Wijesekera et al.,* 1999], and the seventh criterion is therefore needed. The relative impact of temperature and salinity fluctuations on density fluctuations can be expressed as a turbulent density ratio, R_σ, defined by

$$R_\sigma = \frac{\beta}{\alpha}\frac{\sigma_{S'}}{\sigma_{T'}}, \qquad \text{(B2)}$$

where α is the coefficient of thermal expansion, β is the coefficient of saline contraction and $\sigma_{S'}$ and $\sigma_{T'}$ are the standard deviations of the horizontal salinity and temperature gradients respectively (Δx =0.5 m). In the usual definition of the density ratio [e.g. *Turner*, 1979], the standard deviations are replaced by the respective vertical gradients of temperature and salinity. In the above definition, R_σ expresses the relative contribution of high-pass filtered temperature and salinity fluctuations to high-pass filtered fluctuations of density. Spectra of T and S have a slope of approximately -5/3 in a high wave number band (shown below) so that spectra of T' and S' have a slope of +1/3 in the same band with a cutoff at the Nyquist wave number (1 m^{-1}). Because the surface is cooled by at least 100 W m^{-2}, we expect the fluctuations T' and S' to be turbulent.

To calculate R_σ, it was necessary to correct the standard deviations of T' and S' which appear in (B2). The response of the temperature sensor was significantly attenuated at wave numbers approaching the Nyquist wave number which led to an underestimate of $\sigma_{T'}$, defined in spectral terms by

$$\sigma^2_{T'} = \int_{k_0}^{k_N} S_{T'}(k)dk, \qquad \text{(B3)}$$

where $S_{T'}(k)$ is the spectrum of T', k_0 is the inverse of the record length (1/2000 m for the segments analyzed here), and k_N is the Nyquist wave number (1 m^{-1}). The magnitude of the correction was estimated from the spectrum of 70 km (5 hours) of bow temperature data containing 20 km of a fresh surface anomaly produced by rainfall (*Wijesekera et al.*, 1999, Figure 13, hereinafter WPH13). The wind was a nearly constant 10 m s^{-1} and surface cooling averaged 225 W m^{-2} for the 5-hour observation period. The magnitude of the correction is the ratio of the area under the spectrum with slope 1/3 to the area under the spectrum of T' ((B3) and WPH13). The correction factor is 2.3. Note that the log-log spectral plots shown in WPH13 are not area preserving, i.e., equal areas under the curves do not contribute equally to the variance (equation (B3)).

The standard deviation of S', which appears in the numerator of R_σ (equation (B3)), must also be corrected because of high-wave number noise introduced by the calculation of salinity from measurements of temperature and conductivity. The noise results from the different response times of the temperature and conductivity sensors at high wave numbers [*Gregg and Hess*, 1985; *Lueck et al.*, 1977; *Morison et al.*, 1994]. The correction is calculated in a manner similar to the correction for the variance of T' and is 0.37.

The correction factors for the variances of T' and S' can be combined to obtain a correction factor for R_σ: $(0.37/2.3)^{1/2} = 0.4$. The true correction factor for a particular segment will depend on signal-to-noise ratios of the temperature and conductivity measurements. The correction factor estimated here is expected to be representative because the observations used to determine the factor are roughly representative (strong surface cooling with and without the effects of rainfall).

For the effect of salinity on density fluctuations to be negligible, we expect that the value of R_σ should be of order 0.1 if it were free of noise. To refine this criterion, we examine the histogram of R_σ (Figure B2). The histogram shows a peak at R_σ equals 0.51 with a rapid decrease for values of R_σ less than 0.46 and greater than 0.64. There are no values of R_σ less than 0.40 because there is a lower bound on $\sigma_{S'}$ due to measurement noise. The noise in S' can be estimated from the minimum measured value of $\sigma_{S'}$ which was 0.0015 psu. We assigned a value of $R_\sigma = 0.44$ as a mean lower bound of R_σ associated with noise in S'. We chose to neglect segments with R_σ greater than 0.64 because they may have been affected by rainfall. The effective value of R_σ for neglect of segments was obtained by subtracting the lower noise bound (0.44) from 0.64 to obtain 0.20 which agrees with the requirement that R_σ should be of order 0.1. Application of the criterion (after applying the previous six criteria) removed 10 segments and we are left with a total of 306 segments for analysis. For the accepted segments, $\sigma_{S'}$ does not exceed 0.0031 psu, approximately twice the estimated noise floor (0.0015 psu).

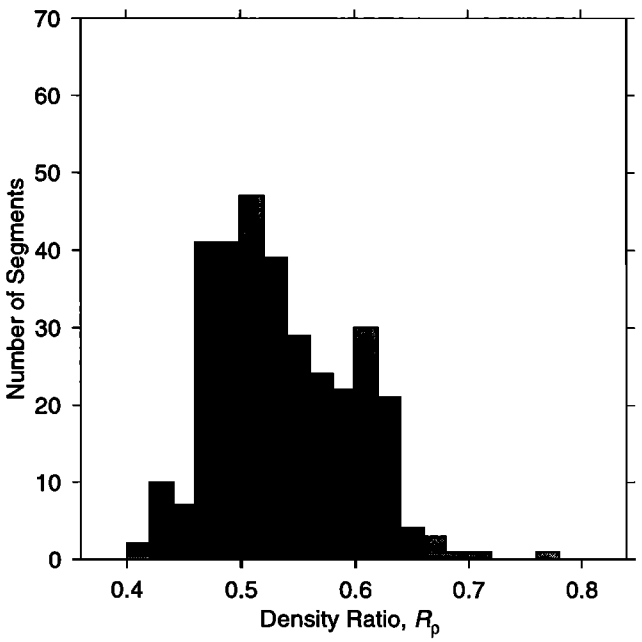

Figure B2. Histogram of the turbulent density ratio R_ρ as defined in (B2).

Appendix C: Mixed Layer Depth

Estimates of mixed layer depth (D) were made for 1-dbar vertical and 2-nm horizontal averages of Seasoar upcasts of σ_θ [*Huyer et al.*, 1997]. Each 2-nm interval included one or two upcasts. Downcasts were not used because the rapid descent rate of the CTD on the downcasts made estimates of salinity and density less reliable than on the upcasts. The average time of the upcast observations in the upper 100 dbar was assigned to each estimate of D. D was calculated for each average upcast by reordering the σ_θ profile to make it statically stable or neutral and then finding the deepest depth at which the difference between σ_θ at that depth and the uppermost observation (typically in the upper 5 m) was less than a prescribed $\Delta\rho$. Estimates of D were made for $\Delta\rho$ equal 0.01 and 0.02 kg m^{-3} and the smaller $\Delta\rho$ was used to determine D in this investigation. $\Delta\rho$ equal 0.01 corresponds to the definition of D used by other investigators [e.g., *Peters et al.*, 1986] and there is evidence from microstructure profiles that this definition corresponds to the depth of active mixing [*Wijesekera and Gregg*, 1996; *Smyth et al.*, 1996].

The estimates of D that bracketed and occurred within segments accepted for analysis were analyzed to determine criteria for rejecting possibly erroneous estimates of D. One possible source of error in the estimates of D is that horizontal variations in σ_θ influence the estimate of D. Estimates of D were rejected if the uppermost measurement of density was at a depth in excess of either the previous or the following estimate of D; i.e., the estimate was rejected if the depth of the uppermost measurement of σ_θ may have been at a depth greater than the actual mixed layer depth. Application of this criterion resulted in the rejection of three estimates of D. Estimates of D were also rejected if the difference between the estimates with $\Delta\rho$ equal 0.01 and 0.02 kg m^{-3} exceeded 10 m and the change in D from the previous and following estimates exceeded 10 m. Four estimates were rejected as the result of applying these criteria.

The estimates of D were analyzed to determine uncertainties in the estimates. Linear fits to the accepted estimates of D were computed for each night. On some nights, there was a significant trend in D due to the gradual deepening of the mixed layer. The rms departure of the estimates of D from the linear fits is 4.2 m, which represents an estimate in the uncertainty of the estimates. This estimate of uncertainty is an upper bound because real variations in D, e.g. due to internal waves, contribute to the departures from the fits. The average difference in the estimates of D with $\Delta\rho$ equal 0.01 and 0.02 is 3.7 m, which is a measure of uncertainty associated with the choice of $\Delta\rho$.

Acknowledgments. The efforts of Eric Firing, Peter Hacker, Michael Kosro, and Roger Lukas in obtaining the *Wecoma* observations on which this paper is based are gratefully acknowledged. We also appreciate the efforts of all of the participants on *Wecoma* cruises during COARE. We thank Lynn deWitt for analysis of the *Wecoma* meteorological observations and Chris Fairall for supplying the *MoanaWave* air-sea fluxes. Conversations with Alexander Soloviev are appreciated. This work was supported by the Ocean Sciences Division of the National Science Foundation under grants OCE-9113510, OCE-9525858, and OCE-9907404.

References

Agrawal, Y. C., E. A. Terray, M. A. Donelan, P. A. Hwang, A. J. Williams III, W. M. Drennan, K. K. Kahma, and S. A. Kitaigorodskii, Enhanced dissipation of kinetic energy beneath surface waves, *Nature, 359,* 219–220, 1992.

Alados-Arboledas, L., J. Vida, and J. I. Jimenez, Effects of solar radiation on the performance of pyrgeometers with silicon domes, *J. Atmos. Oceanic Technol., 5,* 666–670, 1988.

Anis, A., and J. N. Moum, Surface wave-turbulence interactions: Scaling ϵ near the surface, *J. Phys. Oceanogr., 25,* 2025–2045, 1995.

Businger, J. A., J. C. Wyngaard, Y. Izumi, and E. F. Bradley, Flux-profile relationships in the atmospheric surface layer, *J. Atmos. Sci., 28,* 181–189, 1971.

Drennan, W. M., M. A. Donelan, E. A. Terry, and K. B. Katsaros, Oceanic turbulence dissipation measurements in SWADE, *J. Phys. Oceanogr., 26,* 808–815, 1996.

Dyer, A. J., A review of the flux-profile relationships, *Boundary Layer Meteorol., 42,* 9–17, 1974.

Fairall, C. W., E. F. Bradley, D. P. Rogers, J. B. Edson, and G. S. Young, Bulk parameterization of air-sea fluxes for tropical ocean global atmosphere coupled ocean atmosphere response experiment, *J. Geophys. Res., 101,* 3747–3764, 1996a.

Fairall, C. W., E. F. Bradley, J. S. Godfrey, G. A. Wick, J. B. Edson, and G. D. Young, Cool skin and warm layer effects on sea surface temperature, *J. Geophys. Res., 101,* 1295–1308, 1996b.

Gill, A. E., *Atmosphere-Ocean Dynamics*, 662 pp., Academic, San Diego, California., 1982.

Gregg, M. C., and W. Hess, Dynamics response calibration of Sea-Bird temperature and conductivity sensors, *J. Atmos. Oceanic Technol., 2,* 304–313, 1985.

Gregg, M. C., C. S. Cox, and P. W. Hacker, Vertical microstructure measurements in the central North Pacific, *J. Phys. Oceanogr., 3,* 458–469, 1973.

Godfrey, J. S., R. A. House Jr., R. H. Johnson, R. Lukas, J.-L. Redelsperger, A. Sumi and R. Weller, Coupled Ocean-Atmosphere Response Experiment (COARE): An interim report, *J. Geophys. Res., 103,* 14,395–14,450, 1998.

Huyer, A., P. M. Kosro, R. Lukas, and P. Hacker, Upper-ocean thermohaline fields near 2°S, 156°E during TOGA-COARE, November 1992 to February 1993, *J. Geophys. Res, 102,* 12,749–12,784, 1997.

Kaimal, J. C., and J. J. Finnigan, *Atmospheric Boundary Layer Flows,* 289 pp., Oxford Univ. Press, New York, 1994.

Kaimal, J. C., and J. C. Wyngaard, The Kansas and Minnesota experiments, *Bound.-Layer Meteorol., 50,* 31–47, 1990.

Kaimal, J. C., J. C. Wyngaard, Y. Izumi, and O. R. Cote, Spectral characteristics of surface layer turbulence, *Q. J. R. Meteorol. Soc., 98,* 563–589, 1972.

Kaimal, J. C., J. C. Wyngaard, D. A. Haugen, O. R. Cote, Y. Izumi, S. J. Caughey, and C. J. Reading, Turbulence structure in the convective boundary layer, *J. Atmos. Sci., 33,* 2152–2169, 1976.

Koshmieder, H., Methods and results of definite rain measurements, *Mon. Weather Rev., 62,* 5–7, 1934.

Lueck, R. G., O. Hertzman, and T. R. Osborn, The spectral response of thermistors, *Deep Sea Res., 24,* 951–970, 1977.

Lumley, J. L., and H. A. Panofsky, *The Structure of Atmospheric Turbulence,* 239 pp., Wiley-Interscience, New York, 1964.

Monin, A. S., and A. M. Obukhov, Basic laws of turbulence mixing in the atmospheric surface layer, *Trudy Geofiz. Inst. Akad. Nauk SSSR. 24*(151), 163–187, 1954.

Morison, J., R. Anderson, N. Larson, E. DAsaro and T. Boyd, The correction for thermal- lag effects in Sea-Bird CTD data, *J. Atmos. Oceanic Technol., 11,* 1151–1164, 1994.

Paulson, C. A., and J. J. Simpson, Irradiance measurements in the upper ocean, *J. Phys. Oceanogr., 7,* 952–956, 1977.

Peltier, L. J., J. C. Wyngaard, S. Khanna, and J. G. Brasseur, Spectra in the unstable surface layer, *J. Atmos. Sci., 53,* 49–61, 1996.

Peters, H., M. C. Gregg, and J. M. Toole, On the parameterization of equatorial turbulence, *J. Geophys. Res., 93,* 1199–1281, 1988.

Smyth, W. D., D. Hebert, and J. N. Moum, Local ocean response to a multiphase westerly wind burst, Part I, The dynamic response, *J. Geophys. Res., 101,* 22,495–22,512, 1996.

Soloviev, A., R. Lukas, P. Hacker, H. Schoeberlein, M. Baker, and A. Arjannikov, A near- surface microstructure sensor system used during TOGA COARE, Part II, turbulence measurements, *J. Atmos. Oceanic Technol., 16,* 1598–1618, 1999.

Tennekes, H., and J. Lumley, *A First Course in Turbulence,* 300 pp., MIT Press, Cambridge, Mass., 1983.

Terray, E. A., W. M. Donelan, Y. C. Agrawal, W. M. Drennan, K. K. Kahma, A. J. Williams III, P. A. Hwang, and S. A. Kitaigorodskii, Estimates of kinetic energy dissipation under breaking waves, *J. Phys. Oceanogr., 26,* 792–807, 1996.

Turner, J. S., *Buoyancy Effects in Fluids,* 368 pp., Cambridge Univ. Press, New York, 1979.

Weller, R. A., and S. P. Anderson, Surface meteorology and air-sea fluxes in the Western equatorial Pacific warm pool during the TOGA Coupled Ocean-Atmosphere Response Experiment, *J. Clim., 9,* 1959–1990, 1996.

Wijesekera, H. W., and M. C. Gregg, Surface layer response to weak winds, westerly bursts, and rain squalls in the western Pacific Warm Pool, *J. Geophys. Res., 101,* 977–997, 1996.

Wijesekera, H. W., C. A. Paulson, and A. Huyer, The effect of rainfall on the surface layer during a westerly wind burst in the western equatorial Pacific, *J. Phys. Oceanogr., 29,* 612–632, 1999.

Wyngaard, J. C., On surface-layer turbulence, *Workshop on Micrometeorology,* edited by D. A. Haugen, 392 pp., Am. Meteorol. Soc., Boston, Mass, 1973.

Wyngaard, J. C., and O. R. Cote, The budgets of turbulent kinetic energy and Temperature variance in the atmospheric surface layer, *J. Atmos. Sci., 28,* 190–210, 1971.

A. Huyer, C. A. Paulson, and H. W. Wijesekera, College of Oceanic and Atmospheric Sciences, Oregon State University, Corvallis, OR 97331-5503, USA. (ahuyer@oce.orst.edu; hemantha@oce.orst.edu; cpaulson@oce.orst.edu)

(Received August 31, 2000; revised April 10, 2001; accepted April 26, 2001.)